Supplementary material

On the complete interface development for Al/Cu magnetic pulse welding via experimental characterizations and multiphysics numerical simulations

J.S. Li [1], T. Sapanathan [2,*], R.N. Raoelison [3], Y.L. Hou [4,**], A. Simar [2], M. Rachik [1]

[1] Université de Technologie de Compiègne, CNRS, Roberval (Mechanics, energy and electricity), Centre de recherche Royallieu - CS 60319 - 60203 Compiègne cedex, France

[2] UCLouvain, Institute of Mechanics, Materials and Civil Engineering, IMAP, 1348 Louvain-la-Neuve, Belgium

[3] Université de Bourgogne Franche-Comté - UTBM, Laboratoire Interdisciplinaire Carnot de Bourgogne, UMR 6303 CNRS, 90100 Belfort, France

[4] School of Mechanical and Power Engineering, Zhengzhou University, Science Road 100, 450001 Zhengzhou, China

Corresponding author: * Thaneshan Sapanathan (thaneshan.sapanathan@uclouvain.be);
** Yuliang Hou (yulianghou@zzu.edu.cn)

This document contains:

Governing equations of coupled electromagnetic-mechanical model

The electromagnetic step involves the calculation of magnetic field and eddy current governed by the Maxwell's equations, electrical and magnetic constitutive relations, respectively given by Eqs (1-4), (5) and (6).

$$\vec{\nabla} \times \vec{E} = -\frac{\partial \vec{B}}{\partial t} \quad (1)$$

$$\vec{\nabla} \times \vec{H} = \vec{J} + \varepsilon \frac{\partial \vec{E}}{\partial t} \quad (2)$$

$$\vec{\nabla} \times \vec{B} = 0 \quad (3)$$

$$\vec{\nabla} \times \vec{B} = \frac{\rho}{\varepsilon} \quad (4)$$

$$\vec{J} = \sigma \vec{E} + \vec{J_s} \quad (5)$$

$$\vec{B} = \mu \vec{H} \quad (6)$$

where, $\vec{E}$, $\vec{B}$, $\vec{H}$, $\vec{J}$, ε, ρ, σ, $\vec{J_s}$, and μ respectively denote electric field, magnetic flux density, magnetic field intensity, total current density, electrical permittivity, total charge density, electrical conductivity, source current density, magnetic permeability. During the MPW process, there is no charge accumulation and eddy current approximation follow a divergence free current density, therefore, $\rho = 0$ and $\varepsilon \frac{\partial \vec{E}}{\partial t} = 0$.

Thus, Eq. (1) and (3) provide the following correlations given by Eq. (7) and (8), respectively, due to their divergence condition.

$$\vec{E} = -\vec{\nabla}\emptyset - \frac{\partial \vec{A}}{\partial t} \quad (7)$$

$$\vec{B} = \vec{\nabla} \times \vec{A} \quad (8)$$

where, $\emptyset$ and $\vec{A}$ represent the electric scalar potential and the magnetic vector potential, respectively. As the mathematical degree of freedom is fulfilled with the magnetic vector potential $\vec{A}$, hence, a gauge equation is applicable. Then, combining the aforementioned co-relations and the generalized Coulomb gauge condition, $\nabla(\sigma\vec{A}) = 0$, the vector and scalar potentials can separately be described by Eq. (9) and (10), respectively.

$$\nabla(\sigma\vec{\nabla}\emptyset) = 0 \tag{9}$$

$$\sigma\frac{\partial\vec{A}}{\partial t} + \vec{\nabla}\times\left(\frac{1}{\mu}\vec{\nabla}\vec{A}\right) + \sigma\vec{\nabla}\emptyset = \vec{J_s} \tag{10}$$

By solving Eqs. (9) and (10), we can obtain the two unknowns $\vec{A}$ and $\emptyset$ in the electromagnetic system. Finally, the Lorentz force can be estimated based on these solutions procedure and magnetic pressure calculations.

The Johnson-Cook model was used in the electromagnetic-mechanical model to describe the high strain constitutive model for the workpieces (Flyer and rod). The input parameters for Johnson-Cook model are identical for the Eulerian model, which are provided in Table S2. Other parts in the assembly (coil, fieldshaper and shock sleeve) were defined with simple elastic properties. Mechanical and electromagnetic properties for all the parts used in the electromagnetic simulation are provided in Table S1.

Table S1: Mechanical and electromagnetic properties of materials used in the electromagnetic-mechanical simulation model

Material	Part	Density (kg/m^3)	Young's modulus (GPa)	Poisson's ratio	Electrical conductivity ($10^7 S/m$)
Al6060-T6	Flyer	2700	68	0.33	3.13
Copper	Rod	8900	124	0.33	3.48
CuBe2	Fieldshaper	8200	125	0.29	1.45
Siclanic®	Coil	8900	130	0.29	2.67
Polymer	Shock sleeve	2700	13	0.29	Non

Table S2: Material properties assigned in the thermo-mechanical model (Gupta et al., 2006 and Gupta et al., 2019).

Material property	Description	Unit	Al6060-T6	Copper
A	Initial yield strength	MPa	148	89
B	Hardening coefficient	MPa	345	291
C	Strain rate constant	-	0.001	0.025
n	Strain hardening exponent	-	0.183	0.31
m	Softening exponent	-	0.895	1.09
T_o	Reference temperature	K	298	298
T_m	Melting temperature	K	916	1356
s	Slope of linear Rankine–Hugoniot's law	-	1.37	1.49
$\gamma 0$	Mie-Grüneisen's coefficient	-	2.14	2.02
G	Shear modulus	GPa	26.2	46.3
$\rho 0$	Reference density	Kg/m^3	2700	8900
Cp	Specific heat capacity	J/(Kg K)	900	385
λ	Thermal conductivity	W/(m K)	237	387

Fig. S1. Prediction of the final weld shape comparing the experimental interface morphology with the numerical simulation.

The coupled electromagnetic-mechanical model (CEMM) was thoroughly validated based on the final geometry under various welding conditions, as shown in Fig. S1. The cross-sections obtained from numerical prediction and experiment for Al/Cu weld are given in Fig. S1 (a) and (b), respectively. The predicted weld geometry agrees well with the experimental observation. It is confirmed via comparing the radii of the outer and inner surfaces of the flyer and flyer thickness from experimental observation and numerical prediction as shown in Fig. S1 (c) and (d), respectively. Thus, we use the predictions from CEMM to investigate the local impact conditions during the MPW process.

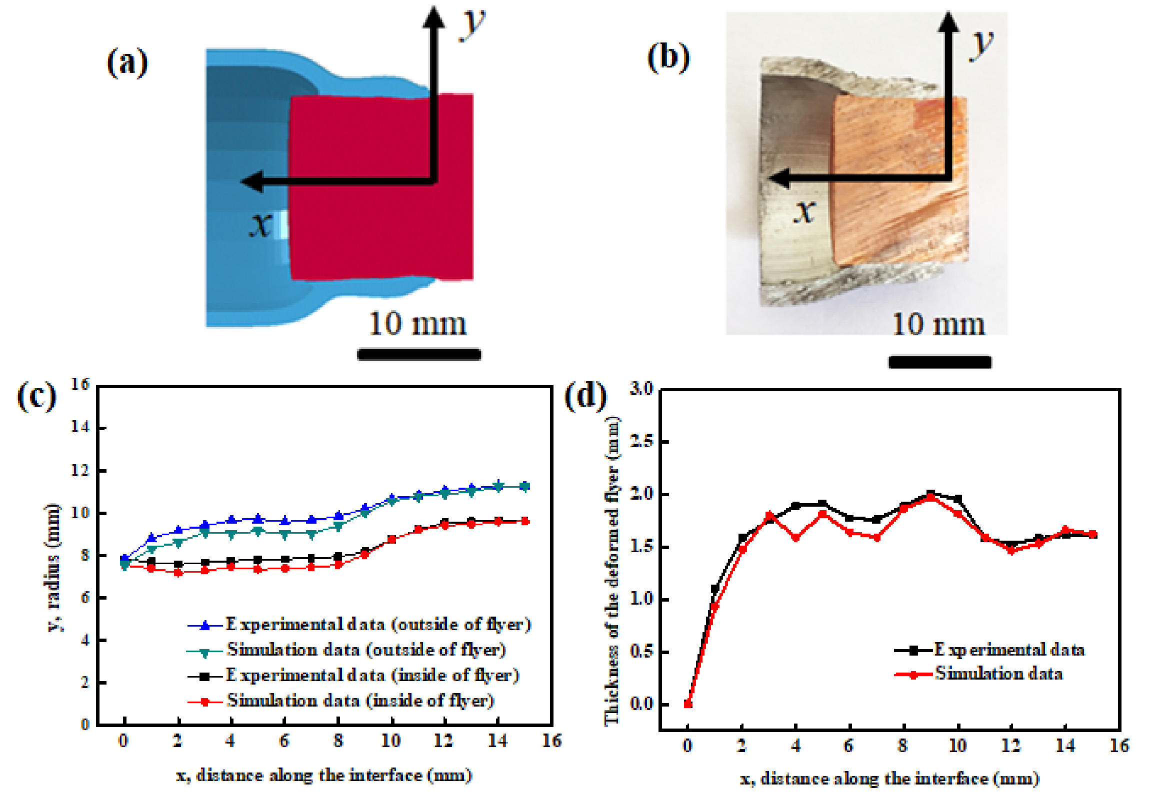

Fig. S1, Cross-section obtained from (a) the end of the simulation and (b) experiment for Al/Cu weld. It should be noted that the lengths of the samples are not the same in (a) and (b), in (a) the excess lengths in the rod and the tube are omitted to reduce the computational cost and (b) is limited to the characterized welded zone only by removing the excess lengths of the rod and tube. Comparison of experimental and predicted results; (c) final inner and out radii of the tube along the x- direction and (d) flyer thickness along the x- direction.

Fig. S2. Eulerian simulation results showing the development of Type 1 wave.

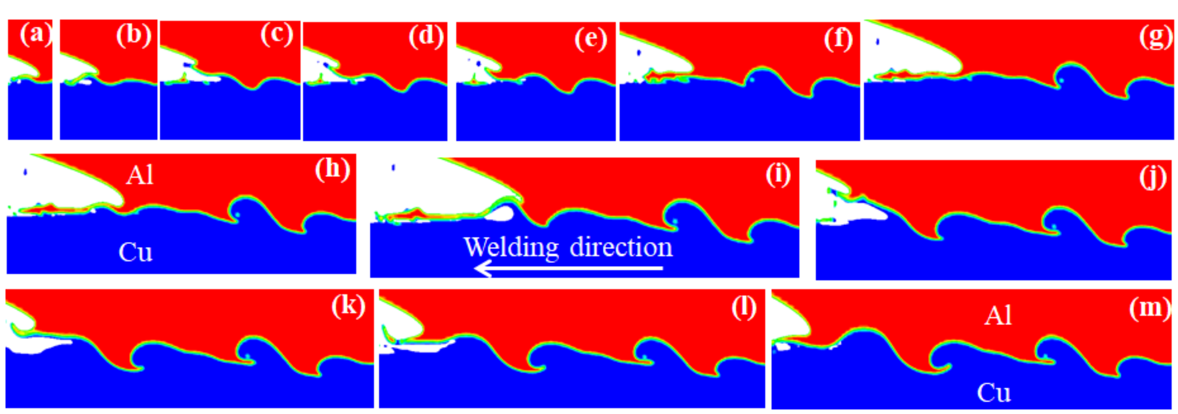

Fig. S3. Eulerian simulation results showing the development of Type 3 wave.

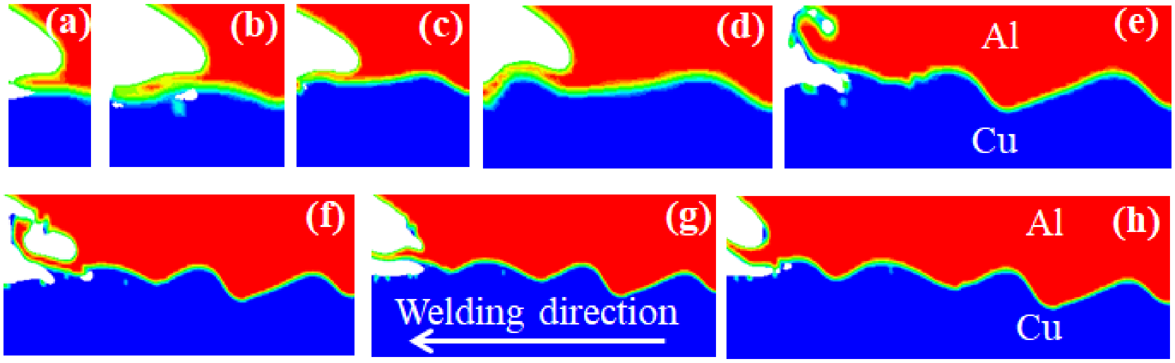

Fig. S4. Eulerian simulation results showing the development of Type 4 wave.

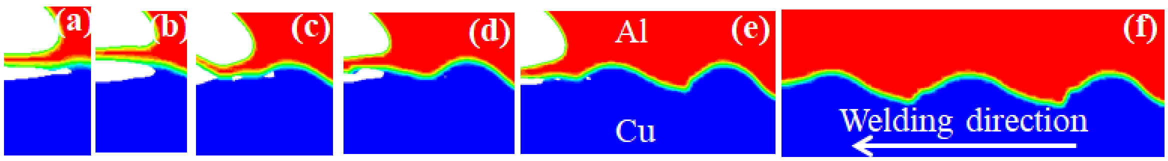

Fig. S5. Pressure distribution in MPa obtained from Eulerian model corresponding to the distance 5.56 mm in Fig. 12 of the main manuscript.

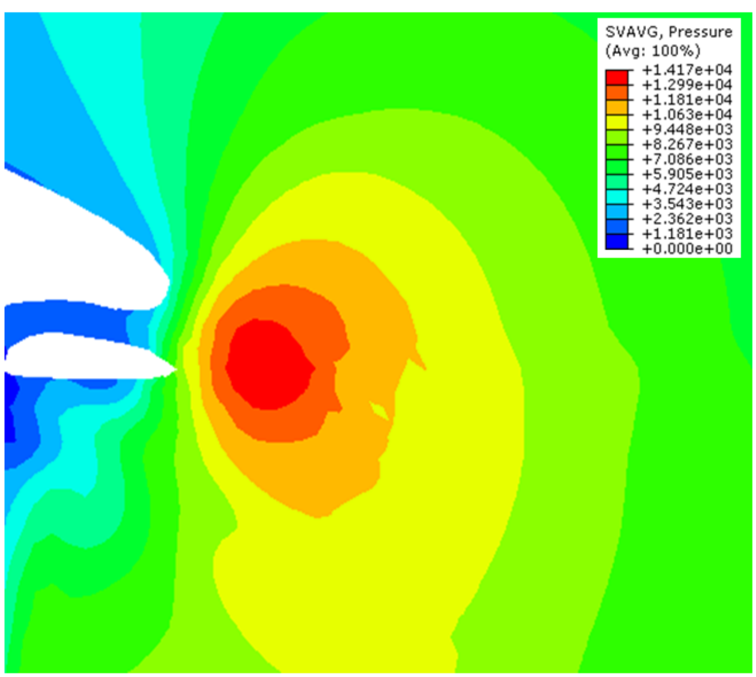

References

Gupta, N.K., Iqbal, M.A., Sekhon, G.S., 2006. Experimental and numerical studies on the behavior of thin aluminum plates subjected to impact by blunt- and hemispherical-nosed projectiles. Int. J. Impact Eng. 32, 1921–1944. https://doi.org/10.1016/J.IJIMPENG.2005.06.007

Gupta, V., Lee, T., Vivek, A., Choi, K.S., Mao, Y., Sun, X., Daehn, G., 2019. A robust process-structure model for predicting the joint interface structure in impact welding. J. Mater. Process. Technol. 264, 107–118. https://doi.org/10.1016/J.JMATPROTEC.2018.08.047